

Dynamic Dictionary Learning for Remote Sensing Image Segmentation

Xuechao Zou^{1,*}, Yue Li^{2,*}, Shun Zhang², Kai Li³,
Shiying Wang², Pin Tao^{2,3}, Junliang Xing³, Congyan Lang^{1,†}

¹School of Computer Science and Technology, Beijing Jiaotong University, Beijing, China

²Department of Computer Technology and Applications, Qinghai University, Xining, China

³Department of Computer Science and Technology, Tsinghua University, Beijing, China

Abstract

Remote sensing image segmentation faces persistent challenges in distinguishing morphologically similar categories and adapting to diverse scene variations. While existing methods rely on implicit representation learning paradigms, they often fail to dynamically adjust semantic embeddings according to contextual cues, leading to suboptimal performance in fine-grained scenarios such as cloud thickness differentiation. This work introduces a dynamic dictionary learning framework that explicitly models class ID embeddings through iterative refinement. The core contribution lies in a novel dictionary construction mechanism, where class-aware semantic embeddings are progressively updated via multi-stage alternating cross-attention querying between image features and dictionary embeddings. This process enables adaptive representation learning tailored to input-specific characteristics, effectively resolving ambiguities in intra-class heterogeneity and inter-class homogeneity. To further enhance discriminability, a contrastive constraint is applied to the dictionary space, ensuring compact intra-class distributions while maximizing inter-class separability. Extensive experiments across both coarse- and fine-grained datasets demonstrate consistent improvements over state-of-the-art methods, particularly in two online test benchmarks (LoveDA and UAVid). Code is available at <https://anonymous.4open.science/r/D2LS-8267/>.

1. Introduction

Remote sensing image segmentation aims to partition scenes into semantically consistent regions, supporting critical applications such as environmental monitoring [21], disaster assessment [18], and urban management [57]. Traditional methods often fail to address the inherent complexity of remote sensing data, including fine-grained structural

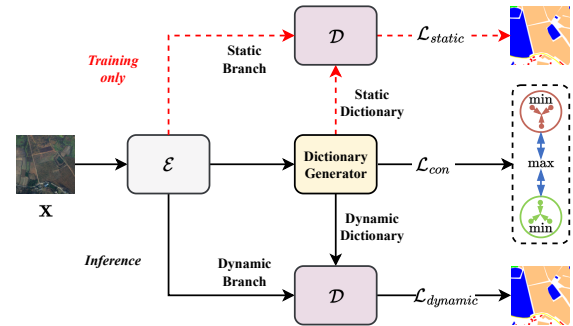


Figure 1. Overall pipeline of our dynamic dictionary learning. “ \mathcal{E} ” and “ \mathcal{D} ” denote the encoder and decoder, respectively.

variations [56] (e.g., thin and thick clouds), intra-class heterogeneity (e.g., varying cloud textures), and inter-class homogeneity (e.g., farmland and grassland) [20].

Current research in remote sensing image segmentation has mainly explored three core directions. CNN-based methods like Hi-ResNet [6] and CDNet [19, 53] prioritize edge optimization and lightweight design through multi-scale architectures, while Transformer-based models such as DC-Swin [48] leverage global context via self-attention. Hybrid approaches (e.g., UNetFormer [49] and AerialFormer [20]) integrate CNN-Transformer strengths for efficient multiscale feature fusion, addressing challenges like cloud segmentation [12, 27] and domain adaptation [56].

Despite these developments, existing methods still face notable issues when confronted with high intra-class heterogeneity and inter-class similarity in remote sensing images. Specifically, most approaches rely on implicit representation learning, which often fails to adapt to subtle morphological or textural differences, such as differentiating thin vs. thick clouds [56] or distinguishing visually similar urban objects [20]. Furthermore, while attention mechanisms [2, 13, 23, 45] capture global context, they do not inherently ensure discriminative class-specific feature representations, leading to confusion among closely related categories. This limitation becomes more pronounced in

*Equal contribution

†Corresponding author

fine-grained segmentation tasks [14, 56], where even minor appearance variations within a class can significantly affect model performance. These shortcomings highlight the need to encode class-aware embeddings explicitly.

To overcome these limitations, we propose a dynamic dictionary learning framework that explicitly constructs and refines class ID embeddings through iterative interactions between image features and semantic dictionaries. Our key innovations are as follows:

- We propose a dynamic dictionary learning framework that explicitly models class-aware semantic embeddings and leverages a contrastive loss to enhance intra-class compactness and inter-class separability, thereby improving performance, particularly in fine-grained remote sensing image segmentation tasks.
- We develop a modulator to convert the static dictionary into a dynamic one by generating attention maps from high-level semantic features, enabling input-specific adaptation and capturing subtle morphological variations within the same class.
- We design a multi-stage alternating cross-attention query decoder that progressively refines both image features and the semantic dictionary iteratively, facilitating mutual optimization and leading to more accurate and robust segmentation outcomes.

Extensive experiments across both coarse-grained datasets (LoveDA [46], UAVid [37], Potsdam [15], Vaihingen [16]) and fine-grained segmentation tasks (Cloud [14], Grass [56]) demonstrated consistent state-of-the-art performance. Our method exhibits superior generalization capabilities on two online test benchmarks (LoveDA and UAVid, where ground truth annotations are unavailable), further validating its robustness and segmentation effectiveness.

2. Related Work

2.1. Remote Sensing Image Segmentation

Remote sensing image segmentation methods can be categorized as coarse- and fine-grained approaches. Coarse-grained segmentation focuses on large-scale semantic understanding of scenes, such as urban landscapes and land-cover classification. Recent advances have integrated Transformers and convolutional neural networks (CNNs) to capture global context and local details. For example, UNetFormer [49] employs a lightweight ResNet encoder and a Transformer-based decoder for real-time urban scene segmentation, while Hi-ResNet [6] enhances edge details through multiscale branches and class-agnostic edge-aware loss. AerialFormer [20] combined hierarchical Transformers with multi-dilated CNNs to address challenges like object density and intra-class heterogeneity. Other studies, such as BANet [47] and ABCNet [30], further optimized feature fusion and computational efficiency through bilat-

eral context modeling and lightweight architectures.

Fine-grained segmentation targets the precise delineation of objects such as thin and thick clouds. Cloud detection methods often leverage dual-branch architectures to balance spatial details and semantic context. DBNet [36] uses a Transformer-CNN hybrid with mutual guidance modules to refine cloud boundaries, and HRCloudNet [27] integrates hierarchical high-resolution features for complex cloud textures. MCDNet [12] addresses thin cloud detection via dual-perspective change-guided mechanisms. In contrast, lightweight models like SCNN [3] and CDNet series [19, 53] reduce computational costs using shallow networks or attention-based refinement. Recent domain adaptation frameworks, such as KTDA [56], further enhance generalization by aligning features across domains. These methods collectively advance fine-grained segmentation accuracy. However, most existing methods struggle to distinguish morphologically similar classes, resulting in ambiguous predictions for fine-grained scenarios. To address this, we propose a dynamic dictionary learning framework that explicitly models class-aware embeddings, thereby enabling a more robust discrimination of related categories.

2.2. Transformer and Attention Mechanisms

Transformer-based approaches such as DETR [2] reformulate object detection as a set prediction task, eliminating hand-crafted components like anchors and NMS. Subsequent works like DETR-style methods [9, 10, 38, 59] optimize query mechanisms and attention patterns to accelerate convergence and improve accuracy. For segmentation, MaskFormer [7, 8] and unify various segmentation tasks through mask classification, while SegViT [54, 55] and SegFace [39] leverage class tokens for semantic mask generation. These methods demonstrate the Transformer’s versatility in dense prediction tasks.

Attention mechanisms [28, 29, 60, 61] play a pivotal role in enhancing feature discrimination and cross-modal interactions. Channel attention modules like SENet [23], CBAM [51], and ECANet [50] adaptively recalibrate channel-wise features, improving representation capacity. Cross-attention enables dynamic information exchange between heterogeneous data, as seen in CCNet [24] for criss-cross context aggregation. Such mechanisms also drive vision foundational models like Segment Anything [26], which utilizes prompt-based cross-attention for zero-shot segmentation. The synergy of diverse attention variants continues to push the boundaries of visual understanding systems. Inspired by DETR-style approaches and attention mechanisms, we explicitly model semantic labels with a learnable dictionary, further enabling progressive optimization via multi-stage alternating cross-attention, thereby effectively distinguishing morphologically similar classes in remote sensing images.

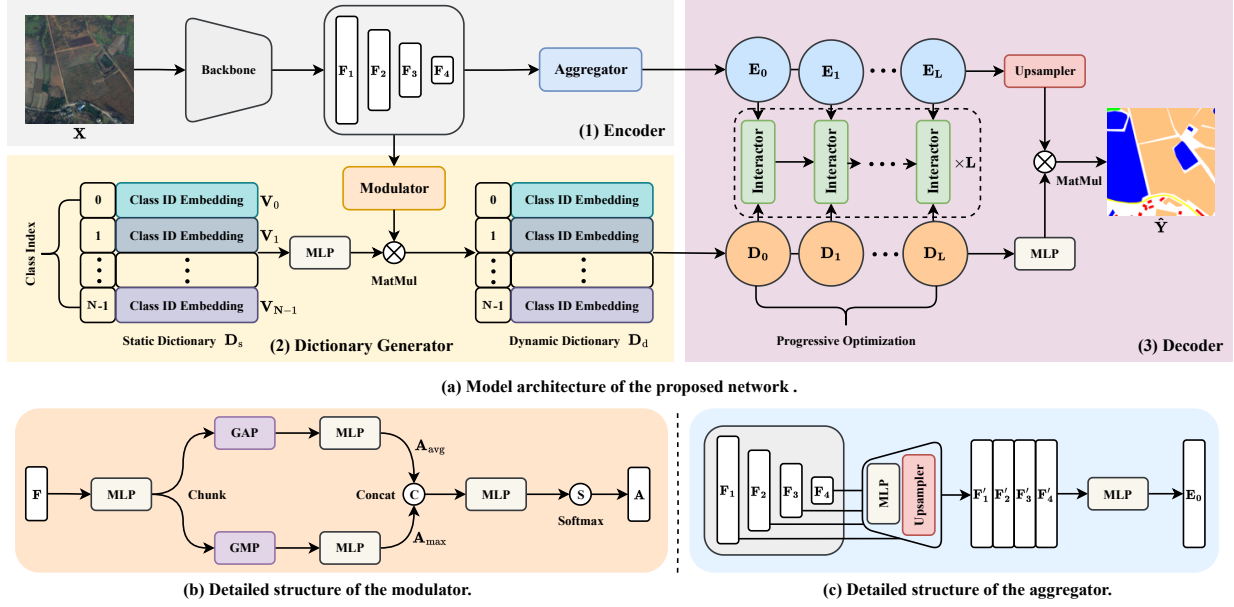


Figure 2. Overview of the proposed network architecture. Notably, we show only the dynamic branch for brevity.

3. Method

3.1. Overall Pipeline

The overall pipeline for dynamic dictionary learning framework (as shown in Fig. 1) can be divided into two key parts: training and inference.

3.1.1. Training

During training, the pipeline employs a dual-branch architecture: the encoder \mathcal{E} processes the input image $\mathbf{X} \in \mathbb{R}^{3 \times H \times W}$ and distributes the extracted features $\mathbf{F} \in \mathbb{R}^{C' \times H' \times W'}$ to two parallel branches: the static and dynamic branches. The static branch generates segmentation maps using a fixed static dictionary produced by a dictionary generator, while the dynamic branch operates with a continuously updated dynamic dictionary throughout training. Both branches share the same decoder. These processes can be formulated as:

$$\mathbf{F} = \mathcal{E}(\mathbf{X}), \quad \mathbf{O}_s = \mathcal{D}(\mathbf{D}_s, \mathbf{F}), \quad \mathbf{O}_d = \mathcal{D}(\mathbf{D}_d, \mathbf{F}), \quad (1)$$

where $\mathcal{E}(\cdot)$ and $\mathcal{D}(\cdot, \cdot)$ denote the encoder and decoder, respectively. $\mathbf{D}_s \in \mathbb{R}^{N \times C'}$ and $\mathbf{D}_d \in \mathbb{R}^{N \times C'}$ represent the static and dynamic dictionaries, while $\mathbf{O}_s \in \mathbb{R}^{N \times H \times W}$ and $\mathbf{O}_d \in \mathbb{R}^{N \times H \times W}$ are the segmentation outputs from the static and dynamic branches. N is the number of semantic categories, H , W , and C' denote the height, width of the image, and the number of feature channels, respectively.

In the training process, we achieve joint optimization by minimizing the loss functions of the static and dynamic branches, namely \mathcal{L}_{static} and $\mathcal{L}_{dynamic}$. The total loss function

is defined as a weighted sum of the individual losses:

$$\mathcal{L}_{total} = \lambda_{static} \cdot \mathcal{L}_{static} + \lambda_{dynamic} \cdot \mathcal{L}_{dynamic}, \quad (2)$$

where $\lambda_{static} = 0.4$ and $\lambda_{dynamic} = 1$ are the default hyper-parameters. During training, the network is optimized by minimizing the total loss \mathcal{L}_{total} .

The loss for the static branch, \mathcal{L}_{static} , is composed of a weighted sum of the cross-entropy loss and the Dice loss, which is a common design in segmentation tasks [25, 39]:

$$\mathcal{L}_{static} = \mathcal{L}_{ce}(\mathbf{O}_s, \mathbf{Y}) + \mathcal{L}_{dice}(\mathbf{O}_s, \mathbf{Y}), \quad (3)$$

where \mathbf{O}_s denotes the segmentation prediction from the static branch, and $\mathbf{Y} \in \mathbb{R}^{N \times H \times W}$ represents the ground truth segmentation label. The cross-entropy loss is employed for per-pixel classification, whereas the Dice loss focuses on the overlapping regions between the predicted and the ground truth segmentation maps, effectively mitigating the class imbalance problem, which is particularly important for segmentation tasks involving long-tail classes.

For the dynamic branch, the loss $\mathcal{L}_{dynamic}$ not only includes the same loss terms as the static branch but also incorporates a dictionary-based contrastive loss [41] to ensure the embedding representations for each class are unique and discriminative. Specifically, the dynamic loss is defined as:

$$\mathcal{L}_{dynamic} = \mathcal{L}_{ce}(\mathbf{O}_d, \mathbf{Y}) + \mathcal{L}_{dice}(\mathbf{O}_d, \mathbf{Y}) + \mathcal{L}_{con}(\mathbf{D}_d). \quad (4)$$

Moreover, the contrastive loss \mathcal{L}_{con} consists of an intra-class compactness loss \mathcal{L}_{intra} and an inter-class dispersion loss \mathcal{L}_{inter} :

$$\mathcal{L}_{con} = \frac{\mathcal{L}_{intra}}{\mathcal{L}_{inter} + \epsilon}, \quad (5)$$

where $\epsilon = 10^{-6}$ is used to prevent division by zero. The intra-class compactness loss measures the average Euclidean distance between the samples and their corresponding class centers:

$$\mathcal{L}_{\text{intra}} = \frac{1}{B \cdot N} \sum_{i=1}^N \sum_{b=1}^B \|\mathbf{D}_d^{(b,i)} - \boldsymbol{\mu}_i\|_2^2, \quad (6)$$

where B denotes the batch size, N is the total number of classes, and $\mathbf{D}_d^{(b,i)}$ represents the embedding of the b -th sample in class i . The class center $\boldsymbol{\mu}_i$ is computed as:

$$\boldsymbol{\mu}_i = \frac{1}{B} \sum_{b=1}^B \mathbf{D}_d^{(b,i)}. \quad (7)$$

The inter-class dispersion loss aims to maximize the pairwise Euclidean distance between different class centers to enhance class separability:

$$\mathcal{L}_{\text{inter}} = \frac{2}{N(N-1)} \sum_{i=1}^{N-1} \sum_{j=i+1}^N \|\boldsymbol{\mu}_i - \boldsymbol{\mu}_j\|_2^2. \quad (8)$$

The double summation iterates over all possible pairs of classes, ensuring adequate separation between them.

3.1.2. Inference

The network uses only the dynamic branch during inference, which utilizes the dynamic dictionary learned during training. The encoder processes the input image and generates feature maps, which are passed to the dynamic branch. The decoder then generates the segmentation maps. The dynamic dictionary complements the static dictionary by adaptively capturing the input-specific patterns, thereby improving the model’s generalization to unseen data.

3.2. Proposed Network

The proposed network architecture (see Fig. 2) consists of an encoder, a dictionary generator, and a decoder, each playing a critical role in extracting features, learning dynamic dictionaries, and generating accurate segmentation maps.

3.2.1. Encoder

The encoder (as shown in Fig. 2a1) is responsible for extracting feature representations from the input image. Initially, the input image \mathbf{X} is processed by a backbone, generating multi-scale feature maps $\{\mathbf{F}_i \in \mathbb{R}^{C_i \times H_i \times W_i}\}_{i=1}^4$, where $W_i = \frac{W}{2^i}$, $H_i = \frac{H}{2^i}$, and $C_i = C \times 2^i$. These feature maps are then passed through the aggregator, which performs feature mapping (Eq. (9)) and aggregation (Eq. (10)). The feature mapping step involves channel transformations, implemented by a multi-layer perceptron (MLP), and up-sample interpolation to align all feature maps to the same dimensionality. After the mapping and interpolation, an MLP

aggregates the features. The final output from the encoder is passed to the dictionary generator and the decoder.

$$\mathbf{F}'_i = \phi(\text{MLP}(\mathbf{F}_i)), \quad i \in \{1, 2, 3, 4\} \quad (9)$$

$$\mathbf{E}_0 = \text{MLP}(\mathbf{F}'_1 \parallel \mathbf{F}'_2 \parallel \mathbf{F}'_3 \parallel \mathbf{F}'_4), \quad (10)$$

where $\{\mathbf{F}'_i \in \mathbb{R}^{C' \times H' \times W'}\}_{i=1}^4$ are the feature maps after feature mapping, and $H' = H_1, W' = W_1$. $\phi(\cdot)$ denotes the interpolation function. “ \parallel ” represents the concatenation operation along the channel dimension, and $\mathbf{E}_0 \in \mathbb{R}^{C' \times H' \times W'}$ is the final aggregated feature map.

3.2.2. Dictionary Generator

The dictionary generator is the core component of the proposed network and is responsible for creating static and dynamic dictionaries used in segmentation. These dictionaries help map feature information to class identifiers, enabling the model to distinguish different classes. The dynamic dictionary adapts during inference by modulating the static dictionary with input-specific attention. Unlike its static counterpart, it adjusts class ID embeddings to capture morphological variations across images, enhancing representation for nuanced inter-class distinctions.

Static Dictionary The static dictionary is a set of class ID embeddings used during the early stages of training. Each class ID embedding is associated with a learnable vector within the static dictionary. Once trained, these vectors are kept constant and do not change with input images, making them “static.” As a result, the static dictionary remains unchanged during inference. The static dictionary can be represented as:

$$\mathbf{D}_s = \{0 : \mathbf{V}_0, 1 : \mathbf{V}_1, \dots, N-1 : \mathbf{V}_{N-1}\}, \quad (11)$$

where $\mathbf{D}_s \in \mathbb{R}^{N \times C'}$ denotes the static dictionary, class index serves as the key, and $\mathbf{V}_i \in \mathbb{R}^{C'}$ represents the embedding vector corresponding to the i -th class, which is the value in the dictionary. N is the number of classes.

Dynamic Dictionary The modulator (Fig. 2b) produces an attention map from encoder features to convert the static dictionary into a dynamic dictionary. The feature map $\mathbf{F} \in \mathbb{R}^{C_i \times H_i \times W_i}$ extracted from the encoder is first processed through an MLP layer. Specifically, we define $\mathbf{F} = \mathbf{F}_4$, which encapsulates high-level semantic information. Subsequently, \mathbf{F} is split along the channel dimension into two separate chunks. One chunk undergoes global average pooling (GAP) followed by an MLP, while the other is processed through global max pooling (GMP) and a separate MLP. The outputs from these two branches are then concatenated

along the channel dimension and fed into another MLP. Finally, the resulting feature representation is normalized using the softmax function, generating the attention map.

$$\mathbf{A}_{\text{avg}} = \text{MLP}(\text{GAP}(\mathbf{F}_{\text{avg}})), \mathbf{A}_{\text{max}} = \text{MLP}(\text{GMP}(\mathbf{F}_{\text{max}})), \quad (12)$$

where $\mathbf{F}_{\text{avg}} \in \mathbb{R}^{\frac{C_i}{2} \times H_i \times W_i}$ and $\mathbf{F}_{\text{max}} \in \mathbb{R}^{\frac{C_i}{2} \times H_i \times W_i}$ represent the two chunks of the feature map \mathbf{F} . After concatenating the results of $\mathbf{A}_{\text{avg}} \in \mathbb{R}^{\frac{C_i}{2}}$ and $\mathbf{A}_{\text{max}} \in \mathbb{R}^{\frac{C_i}{2}}$, the final attention map \mathbf{A} is computed as:

$$\mathbf{A} = \text{Softmax}(\text{MLP}(\mathbf{A}_{\text{avg}} \parallel \mathbf{A}_{\text{max}})), \quad (13)$$

where $\mathbf{A} \in \mathbb{R}^{N \times r}$ denotes the attention map, and $r = 4$ represents the reduced dimensionality. The static dictionary \mathbf{D}_s is then transformed into the dynamic dictionary $\mathbf{D}_0 \in \mathbb{R}^{N \times C'}$ by matrix multiplication with the attention map \mathbf{A} :

$$\mathbf{D}_0 = \text{MLP}(\mathbf{D}_s) \otimes \mathbf{A}, \quad (14)$$

where \mathbf{D}_0 denotes the initial dynamic dictionary, \otimes denotes matrix multiplication. The initial dynamic dictionary is then passed to the decoder for iterative interaction and updates.

3.2.3. Decoder

In the decoder, the dynamic dictionary \mathbf{D}_0 and the image feature map \mathbf{E}_0 interact over \mathbf{L} stages for progressive optimization. During each stage, the dynamic dictionary and image feature alternately perform cross-attention queries, allowing for updates for both. The iterative process is:

$$\begin{aligned} \mathbf{D}_l \in \mathbb{R}^{N \times C'} &= \text{softmax} \left(\frac{\mathbf{D}_{l-1} \mathbf{E}_{l-1}^\top}{\sqrt{d_k}} \right) \mathbf{E}_{l-1}, \quad (\text{D queries E}) \\ \mathbf{E}_l \in \mathbb{R}^{C' \times H' \times W'} &= \text{softmax} \left(\frac{\mathbf{E}_{l-1} \mathbf{D}_l^\top}{\sqrt{d_k}} \right) \mathbf{D}_l, \quad (\text{E queries D}) \end{aligned} \quad (15)$$

where $l \in [1, \mathbf{L}]$ denotes the optimization stage. This alternating mechanism enables mutual enhancement between the dynamic dictionary and image features. Once the final feature map \mathbf{E}_L is obtained after \mathbf{L} stages, the feature map is upsampled. Matrix multiplication is applied between the upsampled feature map and the dictionary \mathbf{D}_L to produce the final segmentation output:

$$\hat{\mathbf{Y}} = \phi(\mathbf{E}_L) \otimes \text{MLP}(\mathbf{D}_L), \quad (16)$$

where $\hat{\mathbf{Y}} \in \mathbb{R}^{N \times H \times W}$ represents the final output.

4. Experiments

4.1. Datasets

We evaluated our method on six remote sensing datasets for semantic segmentation, spanning a range of altitudes from

UAV to satellite imagery. These datasets include coarse-grained (LoveDA [46], UAVid [37], Potsdam [15], Vaihingen [16]) and fine-grained (Cloud [14], Grass [56]) categories. For data splitting and preprocessing, the LoveDA, UAVid, Vaihingen, and Potsdam datasets follow the same protocol as in [25, 49]. In contrast, the Grass and Cloud datasets adopted preprocessing strategies identical to those used in [56]. LoveDA and UAVid are notably used in online test scenarios where ground truth labels are unavailable. For more details, please refer to Appendix A.

4.2. Implementation Details

Experimental Setup We set the size of the class ID embedding to 256 and the frequency of progressive optimization, denoted as \mathbf{L} , to 3. The backbone model was ConvNeXt-Base [33]. The training configuration utilized a batch size of 4, with the random seed fixed at 42 to ensure reproducibility. The optimizer was AdamW [35], with an initial learning rate set to 1×10^{-4} and weight decay set to 0.01. The learning rate was dynamically adjusted using a cosine annealing scheduler. All experiments were conducted on a workstation equipped with NVIDIA A100.

Evaluation Metrics We followed the evaluation protocols of the comparative methods [20, 25]: Overall Accuracy (OA), intersection over union (IoU), F1 score, mean IoU (mIoU), and mean F1 (mF1). mIoU and mF1 are the averages of IoU and F1 scores across all classes. For readability, all metrics are presented in percentage form. Metric details and their formal definitions are provided in Appendix B.

4.3. Ablation Study

Effectiveness of Explicit Class Modeling As quantified in ??, our analysis reveals that implicit representation learning (by removing the dictionary generator) leads to consistent performance degradation (mIoU) across all datasets. The particularly pronounced impact on fine-grained segmentation tasks substantiates the effectiveness of explicit class modeling in the framework. Furthermore, additional ablation studies on the dimensionality of class ID embeddings and the backbone are available in Appendix C.

Static Branch or Dynamic Branch Tab. 1 revealed the complementary roles of loss function in different branches. Using only static loss (static branch) yields limited performance while adding dynamic loss (dynamic branch) improves segmentation performance. The contrastive loss provides critical discrimination power - its inclusion boosts Grass performance by +0.43, with LoveDA/Vaihingen also peaking at 55.27/85.27. These results consistently indicate that dynamic branch is superior to static branch, and that joint optimization of dual branches with the addition of contrastive loss can further enhance segmentation performance.

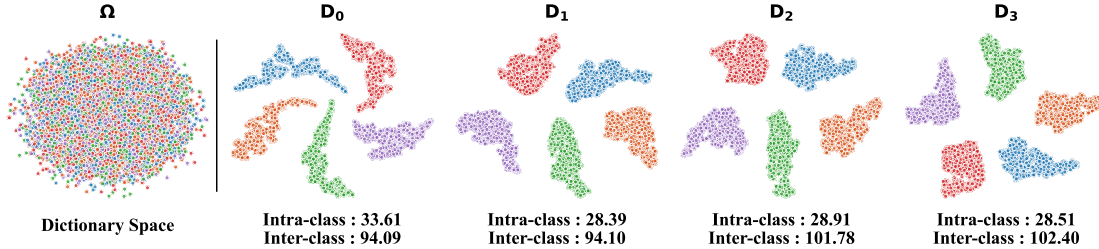


Figure 3. t-SNE visualization of dictionary distributions across different interaction stages.

Table 1. Ablation study on loss function of different branches.

Method	mIoU \uparrow		
	LoveDA	Vaihingen	Grass
$\mathcal{L}_{\text{static}}$	54.80	85.10	50.96
$\mathcal{L}_{\text{dynamic}}$	54.93	85.17	51.38
$\mathcal{L}_{\text{static}} + \mathcal{L}_{\text{dynamic}}$ (w/o \mathcal{L}_{con})	54.95	85.17	51.53
$\mathcal{L}_{\text{static}} + \mathcal{L}_{\text{dynamic}}$ (w/ \mathcal{L}_{con})	55.27	85.27	51.96

Table 2. Performance comparison across interaction stages.

L	mIoU \uparrow				mF1 \uparrow	
	LoveDA	UAVid	Grass	Cloud	Potsdam	Vaihingen
1	54.84	68.79	51.05	83.09	93.29	91.83
2	55.00	69.49	51.21	82.95	94.09	91.88
3	55.27	70.90	51.50	83.10	94.70	91.76
4	54.84	67.88	50.90	80.97	93.87	91.85

Interaction Stages The feature-dictionary interaction stages progressively update class-aware semantic embeddings through multi-stage alternating cross-attention between image features and the dictionary. Experiments in Tab. 2 showed dataset-specific preferences: $L = 3$ yields optimal performance on most datasets, including LoveDA, UAVid, Grass and Cloud, while $L = 2$ suffices for Vaihingen (91.88 mF1). Excessive stages ($L = 4$) reduce segmentation performance on the Cloud dataset, indicating overfitting risks. Visualization of t-SNE (Fig. 3) on the Grass dataset quantifies dictionary evolution: intra-class distances tighten (D_0 : 33.61 \rightarrow D_3 : 28.51), while inter-class distances increase. We selected $L = 3$ as the default, balancing model performance and computational efficiency.

Effectiveness of Each Component We systematically validated the necessity of each component by disabling individual components. As shown in Tab. 3, removing the modulator resulted in the most substantial decline in segmentation performance on the Vaihingen dataset, highlighting its critical role in handling complex urban scenes. Disabling the aggregator leads to the most significant performance drop on the Grass dataset, indicating its importance

for fine-grained feature integration. The interactor contributed consistently across all datasets, demonstrating its capacity to refine ambiguous boundaries. The full model achieved peak performance, proving that these modules provide complementary functionalities rather than isolated improvements. This comprehensive ablation validates that all components are essential for segmentation performance.

Table 3. Effectiveness of each component. Mod., Agg., Int. denote modulator, aggregator, and interaction respectively.

Mod.	Agg.	Int.	mIoU \uparrow		
			LoveDA	Vaihingen	Grass
\times	\checkmark	\checkmark	54.95	85.17	51.35
\checkmark	\times	\checkmark	54.66	82.54	48.52
\checkmark	\checkmark	\times	54.55	85.14	50.95
\checkmark	\checkmark	\checkmark	55.27	85.27	51.96

4.4. Comparison with SOTA Methods

Quantitative Analysis Our method achieved consistent SOTA performance on six remote sensing semantic segmentation benchmarks. It also balances efficiency and performance well, with detailed computational efficiency comparisons (parameter count and FLOPs) in **Appendix D**.

Coarse-grained Segmentation Our method achieved state-of-the-art performance across all coarse-grained datasets. On the LoveDA dataset (Tab. 4), we surpassed SFA-Net by +0.4% mIoU, particularly in challenging categories like agriculture and building. The UAVid results (Tab. 5) further validated our superiority in dynamic urban scenes, achieving 70.9 mIoU by learning distinct representations for different categories. For high-resolution aerial datasets, our approach established new benchmarks on Potsdam and Vaihingen (Tab. 6), with dominant performance in large-scale segmentation scenes.

Fine-grained Segmentation As shown in Tab. 7, our method demonstrates remarkable advantages in distinguishing subtle class variations. On the Grass dataset, we achieve 66.27 mF1, with significant gains in differentiating coverage grades. For the Cloud dataset, our approach establishes an absolute lead, benefiting from the dynamic dictionary’s adaptability to image feature variations. The 89.65 mF1 on

Table 4. Comparison of semantic segmentation performance on the LoveDA dataset.

Method	Background	Building	Road	Water	Barren	Forest	Agriculture	mIoU \uparrow
TransUNet [4]	43.0	56.1	53.7	78.0	9.3	44.9	56.9	48.9
DC-Swin [48]	41.3	54.5	56.2	78.1	14.5	47.2	62.4	50.6
UNetFormer [49]	44.7	58.8	54.9	79.6	20.1	46.0	62.5	52.4
Hi-Resnet [6]	46.7	58.3	55.9	80.1	17.0	46.7	62.7	52.5
AerialFormer [20]	47.8	<u>60.7</u>	59.3	81.5	17.9	<u>47.9</u>	64.0	54.1
SFA-Net [25]	48.4	60.3	59.1	81.9	24.1	46.2	<u>64.0</u>	<u>54.9</u>
Ours	47.6	61.2	<u>59.1</u>	<u>81.6</u>	<u>23.8</u>	48.8	64.8	55.3

Table 5. Comparison of semantic segmentation performance on the UAVid dataset.

Method	Clutter	Building	Road	Tree	Vegetaion	Moving Car	Static Car	Human	mIoU \uparrow
DANet [17]	64.9	58.9	77.9	68.3	61.5	59.6	47.4	9.1	60.6
ABCNet [30]	67.4	86.4	81.2	79.9	63.1	69.8	48.4	13.9	63.8
BANet [47]	66.7	85.4	80.7	78.9	62.1	69.3	52.8	21.0	64.6
SegFormer [52]	66.6	86.3	80.1	79.6	62.3	72.5	52.5	28.5	66.0
UNetFormer [49]	68.4	87.4	81.5	80.2	63.5	73.6	56.4	<u>31.0</u>	67.8
SFA-Net [25]	<u>70.2</u>	<u>89.0</u>	<u>82.7</u>	<u>80.8</u>	<u>64.6</u>	77.5	67.5	30.7	<u>70.4</u>
Ours	71.0	89.7	83.2	82.1	66.1	<u>75.0</u>	<u>59.0</u>	41.4	70.9

Table 6. Comparison of semantic segmentation performance on the Potsdam and Vaihingen dataset.

Method	mF1 \uparrow		
	Potsdam	Vaihingen	Average
DANet [17]	88.9	79.6	84.3
ABCNet [30]	92.7	89.5	91.1
Segmenter [43]	89.2	84.1	86.7
BANet [47]	92.5	89.6	91.1
SwinUpperNet [31]	92.2	89.8	91.0
DC-Swin [48]	93.3	90.7	92.0
UNetFormer [49]	93.5	90.4	92.0
AerialFormer [20]	<u>94.1</u>	90.1	92.1
SFA-Net [25]	93.5	<u>91.2</u>	<u>92.4</u>
Ours	94.7	91.9	93.3

Cloud highlights our capacity to resolve ambiguous boundaries through dynamic dictionary learning. These results collectively confirm that our dynamic dictionary learning paradigm adapts effectively to large-scale scene variations and fine-grained semantic distinctions.

Visualization Results As shown in Fig. 4, our method accurately segments dome-shaped buildings in LoveDA, captures tiny human targets in UAVid without interference from vegetation and clutter, and correctly identifies rough road surfaces in Potsdam despite ground truth mislabeling. Additionally, it enables precise cloud-type separation in Cloud

and enhances vegetation classification in Grass (Fig. 5). More visualization results can be found in Appendix E.

Table 7. Comparison of semantic segmentation performance on the two fine-grained datasets.

(a) Grass		(b) Cloud	
Method	mF1 \uparrow	Method	mF1 \uparrow
FCN [34]	61.99	MCDNet [12]	42.76
PSPNet [58]	62.55	SCNN [3]	52.41
DeepLabV3+ [5]	62.50	CDNetv1 [53]	45.80
UNet [42]	62.34	KappaMask [11]	68.47
SegFormer [52]	62.82	UNetMobv2 [1]	56.91
Mask2Former [8]	58.91	CDNetv2 [19]	70.33
DINOv2 [40]	61.70	HRCLOUDNet [27]	71.36
KTDA [56]	65.01	KTDA [56]	60.08
SFA-Net [25]	<u>65.76</u>	SFA-Net [25]	84.64
Ours	66.27	Ours	89.65

5. Conclusion

In this paper, we propose a dynamic dictionary learning framework to address the limitations of distinguishing similar categories in complex scenes caused by implicit representation learning in remote sensing image segmentation. Our method adaptively models morphological variations while preserving semantic discriminability by iteratively refining class-aware ID embeddings through alternating cross-attention querying and contrastive constraints.

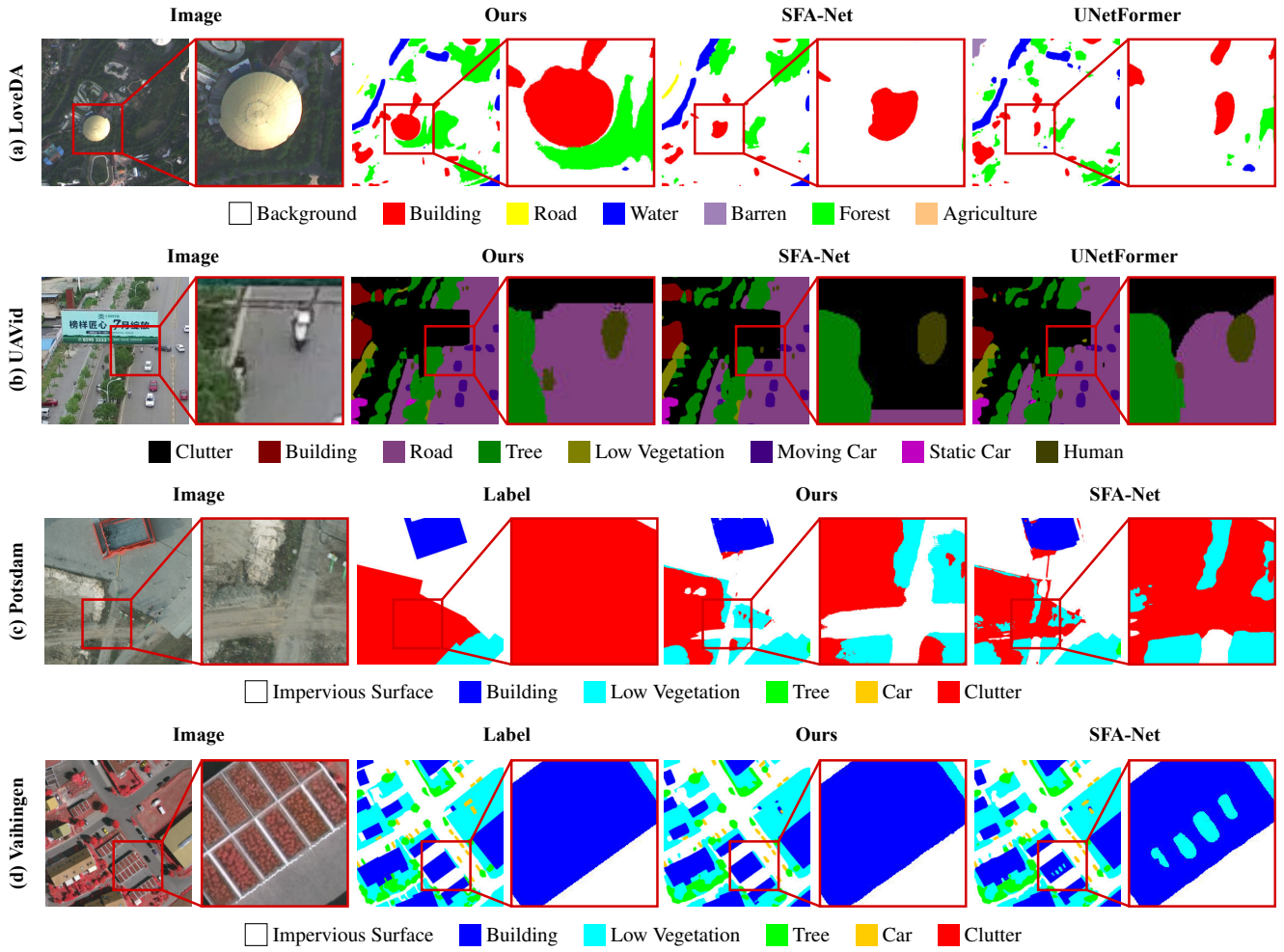


Figure 4. Visualized results on four coarse-grained datasets. Ground truth labels are unavailable in the LoveDA and UAVid datasets.

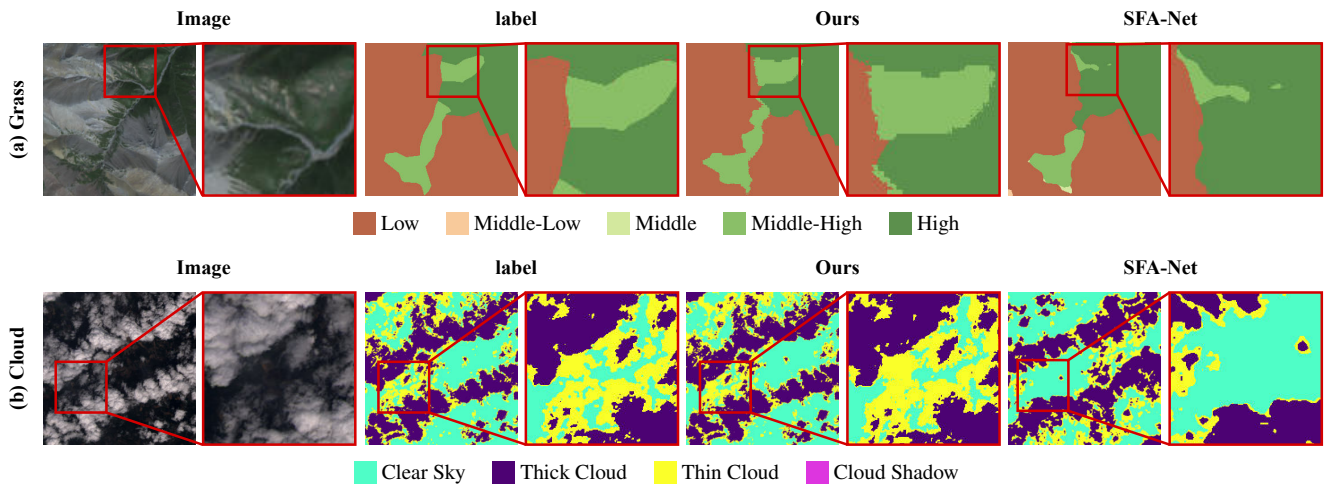


Figure 5. Visualized results on two fine-grained datasets. More visualization of comparative methods can be found in Appendix E.

References

- [1] Cesar Aybar, Luis Yshuaylas, and Jhomira et al. Loja. Cloudsen12, a global dataset for semantic understanding of cloud and cloud shadow in sentinel-2. *Scientific data*, 9(1): 782, 2022. 7
- [2] Nicolas Carion, Francisco Massa, Gabriel Synnaeve, Nicolas Usunier, Alexander Kirillov, and Sergey Zagoruyko. End-to-end object detection with transformers. In *ECCV*, pages 213–229. Springer, 2020. 1, 2
- [3] Dengfeng Chai, Jingfeng Huang, Minghui Wu, Xiaoping Yang, and Ruisheng Wang. Remote sensing image cloud detection using a shallow convolutional neural network. *ISPRS Journal of Photogrammetry and Remote Sensing*, 209: 66–84, 2024. 2, 7
- [4] Jieneng Chen, Jieru Mei, Xianhang Li, Yongyi Lu, Qihang Yu, Qingyue Wei, Xiangde Luo, Yutong Xie, Ehsan Adeli, Yan Wang, et al. Transunet: Rethinking the u-net architecture design for medical image segmentation through the lens of transformers. *Medical Image Analysis*, 97:103280, 2024. 7
- [5] Liang-Chieh Chen, Yukun Zhu, George Papandreou, Florian Schroff, and Hartwig Adam. Encoder-decoder with atrous separable convolution for semantic image segmentation. In *ECCV*, pages 801–818, 2018. 7
- [6] Yuxia Chen, Pengcheng Fang, Xiaoling Zhong, Jianhui Yu, Xiaoming Zhang, and Tianrui Li. Hi-resnet: Edge detail enhancement for high-resolution remote sensing segmentation. *IEEE Journal of Selected Topics in Applied Earth Observations and Remote Sensing*, 17:15024–15040, 2024. 1, 2, 7
- [7] Bowen Cheng, Alex Schwing, and Alexander Kirillov. Per-pixel classification is not all you need for semantic segmentation. *NeurIPS*, 34:17864–17875, 2021. 2
- [8] Bowen Cheng, Ishan Misra, Alexander G Schwing, Alexander Kirillov, and Rohit Girdhar. Masked-attention mask transformer for universal image segmentation. In *CVPR*, pages 1290–1299, 2022. 2, 7
- [9] Yiming Cui, Linjie Yang, and Haichao Yu. Learning dynamic query combinations for transformer-based object detection and segmentation. In *ICML*, pages 6591–6602. PMLR, 2023. 2
- [10] Xiyang Dai, Yinpeng Chen, Jianwei Yang, Pengchuan Zhang, Lu Yuan, and Lei Zhang. Dynamic detr: End-to-end object detection with dynamic attention. In *ICCV*, pages 2988–2997, 2021. 2
- [11] Marharyta Domnich, Indrek Sünter, and Heido et al. Trofimov. Kappamask: Ai-based cloudmask processor for sentinel-2. *Remote Sensing*, 13(20):4100, 2021. 7
- [12] Junwu Dong, Yanhui Wang, Yang Yang, Mengqin Yang, and Jun Chen. Mcdnet: Multilevel cloud detection network for remote sensing images based on dual-perspective change-guided and multi-scale feature fusion. *International Journal of Applied Earth Observation and Geoinformation*, 129: 103820, 2024. 1, 2, 7
- [13] Alexey Dosovitskiy, Lucas Beyer, and Alexander et al. Kolesnikov. An image is worth 16x16 words: Transformers for image recognition at scale. In *ICLR*, pages 1–21, 2020. 1
- [14] Steve Foga, Pat L Scaramuzza, and Song et al. Guo. Cloud detection algorithm comparison and validation for operational landsat data products. *Remote sensing of environment*, 194:379–390, 2017. 2, 5, 12, 13
- [15] International Society for Photogrammetry and Remote Sensing. Posdam datasets. Available online: <https://www.isprs.org/education/benchmarks/UrbanSemLab/2d-sem-label-potsdam.aspx>, 2024. 2, 5, 12, 13
- [16] International Society for Photogrammetry and Remote Sensing. Vaihingen datasets. Available online: <https://www.isprs.org/education/benchmarks/UrbanSemLab/2d-sem-label-vaihingen.aspx>, 2024. 2, 5, 12, 13
- [17] Jun Fu, Jing Liu, Haijie Tian, Yong Li, Yongjun Bao, Zhiwei Fang, and Hanqing Lu. Dual attention network for scene segmentation. In *CVPR*, 2019. 7
- [18] Yibin Fu, Weiming Li, Shuaishuai Fan, Yonghua Jiang, and Hongyang Bai. Cal-net: Conditional attention lightweight network for in-orbit landslide detection. *IEEE Transactions on Geoscience and Remote Sensing*, 61:1–15, 2023. 1
- [19] Jianhua Guo, Jingyu Yang, Huanjing Yue, Hai Tan, Chunping Hou, and Kun Li. Cdnets2: Cnn-based cloud detection for remote sensing imagery with cloud-snow coexistence. *IEEE Transactions on Geoscience and Remote Sensing*, 59(1):700–713, 2021. 1, 2, 7
- [20] Taisei Hanyu, Kashu Yamazaki, Minh Tran, Roy A. McCann, Haitao Liao, Chase Rainwater, Meredith Adkins, Jackson Cothren, and Ngan Le. Aerialformer: Multi-resolution transformer for aerial image segmentation. *Remote Sensing*, 16(16), 2024. 1, 2, 5, 7, 14
- [21] Yassine Himeur, Bhagawat Rimal, Abhishek Tiwary, and Abbes Amira. Using artificial intelligence and data fusion for environmental monitoring: A review and future perspectives. *Information Fusion*, 86-87:44–75, 2022. 1
- [22] Andrew Howard, Mark Sandler, Grace Chu, Liang-Chieh Chen, Bo Chen, Mingxing Tan, Weijun Wang, Yukun Zhu, Ruoming Pang, Vijay Vasudevan, Quoc V. Le, and Hartwig Adam. Searching for mobilenetv3. In *ICCV*, 2019. 14
- [23] Jie Hu, Li Shen, and Gang Sun. Squeeze-and-excitation networks. In *CVPR*, pages 7132–7141, 2018. 1, 2
- [24] Zilong Huang, Xinggang Wang, Lichao Huang, Chang Huang, Yunchao Wei, and Wenyu Liu. Ccnet: Criss-cross attention for semantic segmentation. In *ICCV*, 2019. 2
- [25] Gyutae Hwang, Jiwoo Jeong, and Sang Jun Lee. Sfa-net: Semantic feature adjustment network for remote sensing image segmentation. *Remote Sensing*, 16(17):1–18, 2024. 3, 5, 7, 14
- [26] Alexander Kirillov, Eric Mintun, Nikhila Ravi, Hanzi Mao, Chloe Rolland, Laura Gustafson, Tete Xiao, Spencer Whitehead, Alexander C. Berg, Wan-Yen Lo, Piotr Dollar, and Ross Girshick. Segment anything. In *ICCV*, pages 4015–4026, 2023. 2
- [27] Jingsheng Li, Tianxiang Xue, Jiayi Zhao, Jingmin Ge, Yufang Min, Wei Su, and Kun Zhan. High-resolution cloud detection network. *Journal of Electronic Imaging*, 33(4): 043027–043027, 2024. 1, 2, 7
- [28] Kai Li, Runxuan Yang, and Xiaolin Hu. An efficient encoder-decoder architecture with top-down attention for speech separation. In *ICLR*, pages 1–16, 2023. 2

- [29] Kai Li, Runxuan Yang, Fuchun Sun, and Xiaolin Hu. Iianet: an intra- and inter-modality attention network for audio-visual speech separation. In *ICML*. JMLR.org, 2024. 2
- [30] Rui Li, Shunyi Zheng, Ce Zhang, Chenxi Duan, Libo Wang, and Peter M. Atkinson. Abcnet: Attentive bilateral contextual network for efficient semantic segmentation of fine-resolution remotely sensed imagery. *ISPRS Journal of Photogrammetry and Remote Sensing*, 181:84–98, 2021. 2, 7
- [31] Ze Liu, Yutong Lin, Yue Cao, Han Hu, Yixuan Wei, Zheng Zhang, Stephen Lin, and Baining Guo. Swin transformer: Hierarchical vision transformer using shifted windows. In *ICCV*, pages 10012–10022, 2021. 7, 14
- [32] Ze Liu, Han Hu, Yutong Lin, Zhuliang Yao, Zhenda Xie, Yixuan Wei, Jia Ning, Yue Cao, Zheng Zhang, Li Dong, et al. Swin transformer v2: Scaling up capacity and resolution. In *CVPR*, pages 12009–12019, 2022. 14
- [33] Zhuang Liu, Hanzi Mao, Chao-Yuan Wu, Christoph Feichtenhofer, Trevor Darrell, and Saining Xie. A convnet for the 2020s. In *CVPR*, pages 11976–11986, 2022. 5, 14
- [34] Jonathan Long, Evan Shelhamer, and Trevor Darrell. Fully convolutional networks for semantic segmentation. In *CVPR*, pages 3431–3440, 2015. 7
- [35] Ilya Loshchilov and Frank Hutter. Decoupled weight decay regularization. In *ICLR*, pages 1–18, 2018. 5
- [36] Chen Lu, Min Xia, Ming Qian, and Binyu Chen. Dual-branch network for cloud and cloud shadow segmentation. *IEEE Transactions on Geoscience and Remote Sensing*, 60: 1–12, 2022. 2
- [37] Ye Lyu, George Vosselman, Gui-Song Xia, Alper Yilmaz, and Michael Ying Yang. Uavid: A semantic segmentation dataset for uav imagery. *ISPRS journal of photogrammetry and remote sensing*, 165:108–119, 2020. 2, 5, 12, 13
- [38] Depu Meng, Xiaokang Chen, Zejia Fan, Gang Zeng, Houqiang Li, Yuhui Yuan, Lei Sun, and Jingdong Wang. Conditional detr for fast training convergence. In *ICCV*, pages 3651–3660, 2021. 2
- [39] Kartik Narayan, Vibashan VS, and Vishal M. Patel. Segface: Face segmentation of long-tail classes, 2024. 2, 3
- [40] Maxime Oquab, Timothée Darcet, and Théo et al. Moutakanni. DINOv2: Learning Robust Visual Features without Supervision. *Transactions on Machine Learning Research*, pages 1–31, 2024. 7
- [41] Alec Radford, Jong Wook Kim, Chris Hallacy, Aditya Ramesh, Gabriel Goh, Sandhini Agarwal, Girish Sastry, Amanda Askell, Pamela Mishkin, Jack Clark, et al. Learning transferable visual models from natural language supervision. In *ICML*, pages 8748–8763. PmlR, 2021. 3
- [42] Olaf Ronneberger, Philipp Fischer, and Thomas Brox. U-net: Convolutional networks for biomedical image segmentation. In *MICCAI*, pages 234–241. Springer, 2015. 7
- [43] Robin Strudel, Ricardo Garcia, Ivan Laptev, and Cordelia Schmid. Segmnet: Transformer for semantic segmentation. In *ICCV*, pages 7262–7272, 2021. 7
- [44] Mingxing Tan and Quoc Le. Efficientnetv2: Smaller models and faster training. In *ICML*, pages 10096–10106. PMLR, 2021. 14
- [45] Ashish Vaswani, Noam Shazeer, Niki Parmar, Jakob Uszkoreit, Llion Jones, Aidan N Gomez, Łukasz Kaiser, and Illia Polosukhin. Attention is all you need. *NeurIPS*, 30, 2017. 1
- [46] Junjue Wang, Zhuo Zheng, Ailong Ma, Xiaoyan Lu, and Yanfei Zhong. LoveDA: A remote sensing land-cover dataset for domain adaptive semantic segmentation. In *NeurIPS*, pages 1–17, 2021. 2, 5, 12, 13, 14
- [47] Libo Wang, Rui Li, Dongzhi Wang, Chenxi Duan, Teng Wang, and Xiaoliang Meng. Transformer meets convolution: A bilateral awareness network for semantic segmentation of very fine resolution urban scene images. *Remote Sensing*, 13 (16), 2021. 2, 7
- [48] Libo Wang, Rui Li, Chenxi Duan, Ce Zhang, Xiaoliang Meng, and Shenghui Fang. A novel transformer based semantic segmentation scheme for fine-resolution remote sensing images. *IEEE Geoscience and Remote Sensing Letters*, 19:1–5, 2022. 1, 7
- [49] Libo Wang, Rui Li, Ce Zhang, Shenghui Fang, Chenxi Duan, Xiaoliang Meng, and Peter M. Atkinson. Unetformer: A unet-like transformer for efficient semantic segmentation of remote sensing urban scene imagery. *ISPRS Journal of Photogrammetry and Remote Sensing*, 190:196–214, 2022. 1, 2, 5, 7, 14
- [50] Qilong Wang, Banggu Wu, Pengfei Zhu, Peihua Li, Wangmeng Zuo, and Qinghua Hu. Eca-net: Efficient channel attention for deep convolutional neural networks. In *CVPR*, pages 11534–11542, 2020. 2
- [51] Sanghyun Woo, Jongchan Park, Joon-Young Lee, and In So Kweon. Cbam: Convolutional block attention module. In *ECCV*, pages 3–19, 2018. 2
- [52] Enze Xie, Wenhai Wang, Zhiding Yu, Anima Anandkumar, Jose M. Alvarez, and Ping Luo. Segformer: Simple and efficient design for semantic segmentation with transformers. In *NeurIPS*, pages 12077–12090, 2021. 7
- [53] Jingyu Yang, Jianhua Guo, Huanjing Yue, Zhiheng Liu, Haofeng Hu, and Kun Li. Cdnet: Cnn-based cloud detection for remote sensing imagery. *IEEE Transactions on Geoscience and Remote Sensing*, 57(8):6195–6211, 2019. 1, 2, 7
- [54] Bowen Zhang, Zhi Tian, Quan Tang, Xiangxiang Chu, Xiaolin Wei, Chunhua Shen, et al. Segvit: Semantic segmentation with plain vision transformers. In *NeurIPS*, 2022. 2
- [55] Bowen Zhang, Liyang Liu, Minh Hieu Phan, Zhi Tian, Chunhua Shen, and Yifan Liu. Segvit v2: Exploring efficient and continual semantic segmentation with plain vision transformers. *International Journal of Computer Vision*, 132 (4):1126–1147, 2024. 2
- [56] Shun Zhang, Xuechao Zou, Kai Li, Congyan Lang, Shiyang Wang, Pin Tao, and Tengfei Cao. Knowledge transfer and domain adaptation for fine-grained remote sensing image segmentation, 2025. 1, 2, 5, 7, 12, 13, 14
- [57] Xin Zhang, Yu Liu, Yuming Lin, Qingmin Liao, and Yong Li. Uv-sam: Adapting segment anything model for urban village identification. *AAAI*, 38(20):22520–22528, 2024. 1
- [58] Hengshuang Zhao, Jianping Shi, Xiaojuan Qi, Xiaogang Wang, and Jiaya Jia. Pyramid scene parsing network. In *CVPR*, pages 2881–2890, 2017. 7

- [59] Dehua Zheng, Wenhui Dong, Hailin Hu, Xinghao Chen, and Yunhe Wang. Less is more: Focus attention for efficient detr. In *ICCV*, pages 6674–6683, 2023. [2](#)
- [60] Xuechao Zou, Kai Li, Junliang Xing, Pin Tao, and Yachao Cui. Pmaa: A progressive multi-scale attention autoencoder model for high-performance cloud removal from multi-temporal satellite imagery. In *ECAI*, pages 3165–3172, 2023. [2](#)
- [61] Xuechao Zou, Kai Li, Junliang Xing, Yu Zhang, Shiyang Wang, Lei Jin, and Pin Tao. Diffcr: A fast conditional diffusion framework for cloud removal from optical satellite images. *IEEE Transactions on Geoscience and Remote Sensing*, 62:1–14, 2024. [2](#)

Dynamic Dictionary Learning for Remote Sensing Image Segmentation

Supplementary Material

A. Dataset Details

As shown in Tab. 8, we provide comprehensive and detailed descriptions of all the datasets used in this paper.

LoveDA [46] The LoveDA dataset is a fine-resolution 0.3m dataset designed for urban and rural land cover classification. It consists of 5,987 images, each with a resolution of 512×512 pixels. Captured in three cities—Nanjing, Changzhou, and Wuhan, China—LoveDA spans both urban and rural environments. The metropolitan region contains dense infrastructure and complex geometries, while the rural area features natural landscapes and sparse settlements. This diversity in geographic environments provides valuable data for assessing the adaptability and generalizability of segmentation models. The dataset’s varied land cover improves its versatility for real-world segmentation tasks.

UAVID [37] The UAVID dataset is a high-resolution dataset for semantic segmentation tasks in urban environments. It was captured by an unmanned aerial vehicle (UAV) flying at an altitude of 50 meters and consists of 42 video sequences and 420 images. The images are available in two spatial resolutions: $3,840 \times 2,160$ and $4,096 \times 2,160$ pixels. The dataset includes a diverse range of urban objects, such as buildings, roads, trees, vegetation, vehicles, humans, and other urban clutter. Both top-down and side views of urban scenes are provided, offering a comprehensive perspective for object recognition. In training stage, each image is divided into patches of $1,024 \times 1,024$ pixels.

Potsdam [15] The ISPRS Potsdam dataset consists of 38 drone images from Potsdam, Germany, each with a resolution of 6000×6000 pixels and a ground sampling distance (GSD) of 5 cm, designed for semantic segmentation in urban environments. This dataset is annotated into six categories: impervious surfaces, buildings, low vegetation, trees, cars, and clutter. For the experiments, the images were cropped into $1,024 \times 1,024$ -pixel patches to ensure manageable data processing and to focus on the primary RGB images and their corresponding labels.

Vaihingen [16] The ISPRS Vaihingen dataset includes 33 high-resolution images, each with a pixel resolution of 0.5 m, covering an urban region in Vaihingen, Germany. The images are classified into six categories: impervious surfaces, buildings, low vegetation, trees, cars, and clutter. The dataset’s average image size is $2,494 \times 2,064$ pixels.

For segmentation experiments, we used only the RGB images, and each image was divided into $1,024 \times 1,024$ -pixel patches to facilitate efficient model training and testing.

Cloud [14] The Fine-Grained Cloud Segmentation dataset consists of 96 terrain-corrected (Level-1T) scenes from Landsat 8 OLI and TIRS, covering various biomes. This diverse dataset supports cloud detection and removal tasks in complex environments, offering pixel-level annotations for cloud shadow, clear sky, thin clouds, and cloud areas. Each scene is divided into 512×512 -pixel patches and organized into training, validation, and test sets in a 6:2:2 ratio. The dataset’s wide range of cloud cover types and biomes makes it a valuable resource for training and evaluating segmentation models in cloud detection tasks.

Grass [56] This dataset was developed to overcome the limitations of existing grassland segmentation datasets, such as boundary ambiguity and misclassification in complex terrains. Created using high-resolution satellite imagery from Gaofen-2 and Gaofen-6, it was captured in 2019 over Maduo County, located in the Yellow River source area of China. The dataset includes high-resolution images (8m) and provides detailed grassland coverage classifications across five levels: low coverage, medium-low coverage, medium coverage, medium-high coverage, and high coverage. It consists of 1,500 pairs of 256×256 -pixel patches, with manual refinement to ensure high accuracy. This dataset is especially valuable for fine-grained grassland extraction in high-altitude, ecologically sensitive regions.

B. Evaluation Metrics

Overall Accuracy (OA) calculates the ratio of correct predictions to the total number of pixels:

$$OA = \frac{\sum_i TP_i}{\sum_i (TP_i + FP_i + FN_i)}, \quad (17)$$

where TP_i , FP_i , and FN_i represent true positives, false positives, and false negatives for the i -th class, respectively.

Intersection over Union (IoU) measures the overlap between predicted and ground truth regions for a class. Mean IoU (mIoU) averages the IoU scores across all classes.

$$IoU = \frac{TP}{TP + FP + FN}, \quad (18)$$

Table 8. Overview of remote sensing image datasets for semantic segmentation.

Type	Dataset	Source	GSD ^{*,†}	Patch Size	Category
Coarse Grained	LoveDA [46]	Satellite	0.3m	1024 * 1024	background, building, road, water, barren, forest, agriculture
	UAvid [37]	UAV	50m [†]	1024 * 1024	clutter, building, road, tree, low vegetation, moving car, static car, human
	Potsdam [15]	UAV	5cm	1024 * 1024	impervious surface, building, low vegetation, tree, car, clutter
	Vaihingen [16]	UAV	9cm	1024 * 1024	impervious surface, building, low vegetation, tree, car, clutter
Fine Grained	Cloud [14]	Satellite	30m	512 * 512	cloud shadow, clear sky, thin cloud, thick cloud
	Grass [56]	Satellite	8m	256 * 256	low, medium-low, medium, medium-high, high

* *GSD* (Ground Sampling Distance): The physical pixel size projected onto the ground surface (e.g., 0.3m/pixel = each pixel represents a 0.3x0.3m ground area). Smaller GSD indicates higher spatial resolution.

† For UAvid dataset: The value indicates flight altitude rather than actual GSD. True GSD can be calculated via camera parameters.

$$mIoU = \frac{1}{N} \sum_{i=1}^N IoU_i, \quad (19)$$

where N is the number of classes, and IoU_i is the IoU for the i -th class.

F1 balances precision and recall, providing a harmonic mean of the two. Mean F1 score (**mF1**) averages the F1.

$$F1 = 2 \cdot \frac{\text{Precision} \cdot \text{Recall}}{\text{Precision} + \text{Recall}}, \quad (20)$$

$$mF1 = \frac{1}{N} \sum_{i=1}^N F1_i, \quad (21)$$

where $\text{Precision} = \frac{TP}{TP+FP}$ and $\text{Recall} = \frac{TP}{TP+FN}$. $F1_i$ balances precision and recall for the i -th class.

While OA provides a general performance measure, it is less reliable for imbalanced datasets. In contrast, **IoU** and **F1 score** (and their mean versions, **mIoU** and **mF1**) offer more robust evaluations by considering class-level performance, making them better suited for multi-class tasks.

C. Ablation Study

Dimensions of Class ID Embedding We analyzed the impact of class ID embedding dimensions on segmentation performance. As shown in Fig. 6, increasing dimensions from 64 to 256 boosts performance across all datasets.

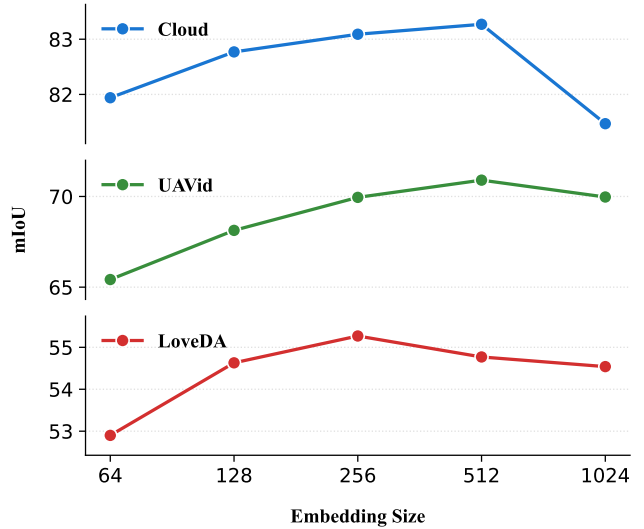


Figure 6. Performance comparison across different class ID embedding sizes for Cloud, UAvid, and LoveDA datasets. The mIoU scores are shown for embedding sizes ranging from 64 to 1024.

While 512 dimensions achieve peak results on UAvid and Cloud, LoveDA slightly degrades, suggesting dimension sensitivity varies with dataset complexity. Extreme dimensions (1024) caused performance collapse, indicating overfitting risks. Therefore, we select 256 as the default value for achieving optimal efficiency-discriminability trade-off.

Table 9. Performance comparison of different backbones under frozen and fully-trained settings on the LoveDA dataset.

Backbone	Status	mIoU \uparrow
ConvNeXt (B) [33]	Frozen	48.50
	Full	55.27
Swin (B) [31]	Frozen	49.76
	Full	53.88
Swinv2 (B) [32]	Frozen	48.43
	Full	54.41
MobileNetv3 (L) [22]	Frozen	46.34
	Full	51.17
EfficientNet (M) [44]	Frozen	44.93
	Full	53.78

Table 10. Computational efficiency comparison with input size 512×512 , including * indicates parameters without backbone.

Method	Params (M)	Params* (M)	Flops (G)
AerialFormer [20]	113.8	26.9	126.8
SFA-Net [25]	10.7	0.6	7.1
KTDA [56]	258.3	170.7	566.4
Ours	<u>90.9</u>	<u>3.3</u>	<u>89.2</u>

Backbone in Encoder We evaluate the impact of different backbone architectures on segmentation performance under frozen and fully trained settings using the LoveDA [46] dataset, as shown in Tab. 9. Among the tested backbones, Swin (B) achieves the highest mIoU of 49.76% in the frozen setting, while ConvNeXt (B) outperforms others with 55.27% when fully trained, demonstrating its superior feature extraction capability when fine-tuned. Swinv2 (B) and Swin (B) exhibit comparable performance, with Swinv2 (B) slightly behind in both settings. MobileNetv3 (L) and EfficientNet (M), being lightweight backbones, yield lower mIoU scores, particularly in the frozen setting, indicating their limited capacity to generalize without fine-tuning. These results suggest that transformer-based backbones generally perform better than CNN-based alternatives, and that full training significantly boosts segmentation performance across all architectures.

D. Computational Efficiency

As shown in Tab. 10, our method achieves a substantial efficiency-performance tradeoff. Excluding the backbone, it has only 3.3M parameters, remaining lightweight. Though SFA-Net [25] has fewer FLOPs, its minimal parameters limit representation capacity. Remarkably, our model achieves significant performance improvements with fewer parameters than both AerialFormer [20] and KTDA [56].

E. More Visualization

Figs. 8 and 9 present comparative visualization results of our method against SFA-Net [25] and UNetFormer [49] across six challenging benchmarks. On the LoveDA (Fig. 8a) and UAVid (Fig. 8b) datasets where test set ground truth is unavailable, our segmentation masks exhibit superior alignment with visual semantics compared to baselines, particularly in preserving structural continuity of buildings and road networks. The Potsdam (Fig. 8c) and Vaihingen (Fig. 8d) results demonstrate our model’s robustness against complex urban patterns, with significantly reduced segmentation artifacts in cluttered areas. Cloud (Fig. 9a) and Grass (Fig. 9b) segmentation further validate our approach’s capability to handle fine-grained texture variations, achieving state-of-the-art boundary precision. A failure mode analysis (Fig. 10) reveals that tiling artifacts persist in UAVid inference due to our sliding window strategy, suggesting directions for future architectural improvements.

F. Training Dynamics

In this section, we present the curves showing how the metrics of our method and SFA-Net [25] change with the training epochs. By comparing the performance across various aspects, we highlight the advantages of our method.

Training Stability As shown in Fig. 7b and Fig. 7f, our method demonstrates superior stability during training. Compared to SFA-Net, our approach exhibits minimal fluctuations and maintains a steady convergence throughout the training process, which reduces the need for extensive hyperparameter tuning, saving computational resources.

Fitting Speed Fig. 7a and Fig. 7e illustrate the faster fitting speed of our method. Our model achieves optimal performance in fewer epochs, while SFA-Net requires more training time to reach similar results. This faster convergence enables more efficient model training.

Final Performance Fig. 7 holistically demonstrates our method’s superiority across all evaluation metrics (subfigures a-f.). The consistent performance advantages visible throughout the training lifecycle – from initial convergence patterns to final stabilized outputs – validate our approach’s end-to-end effectiveness.

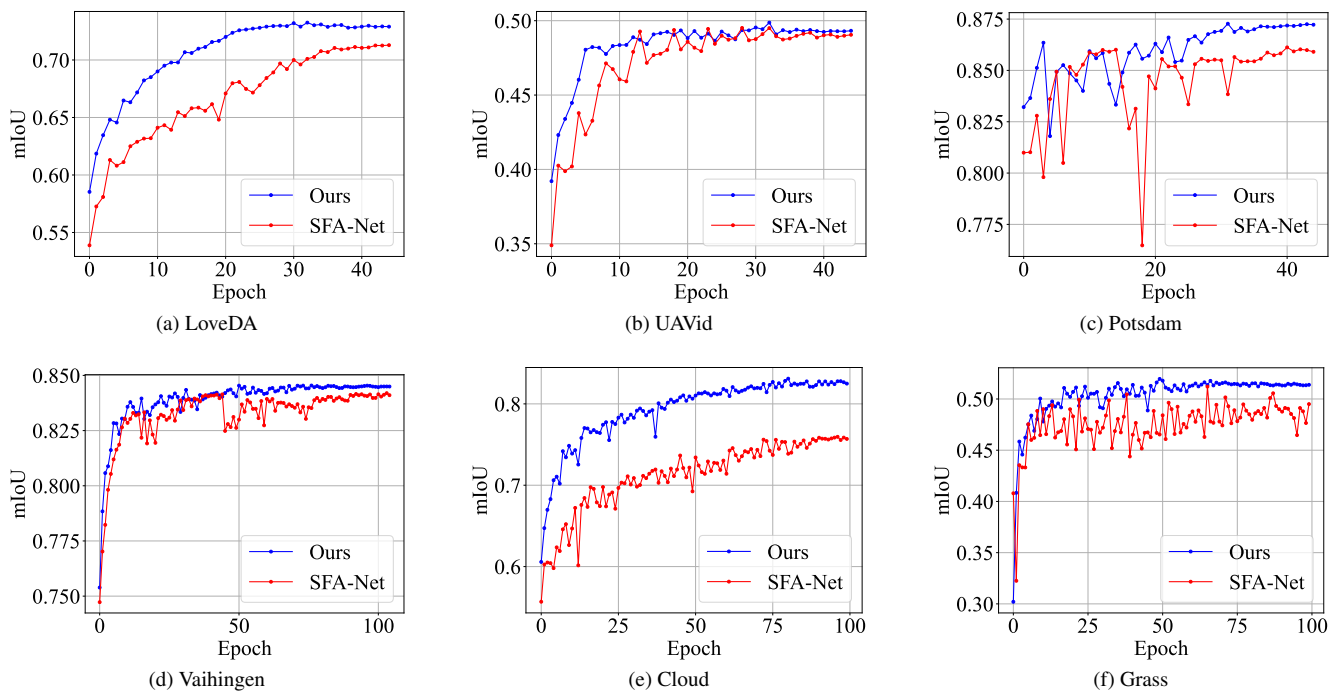
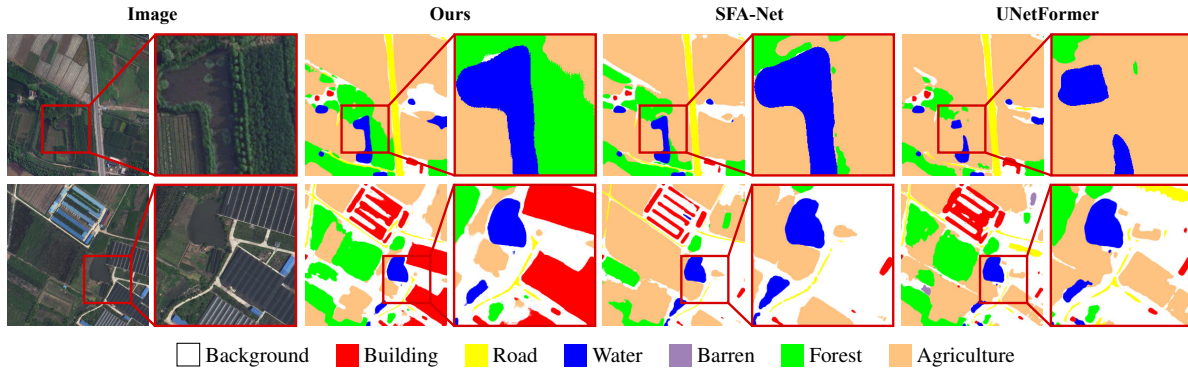
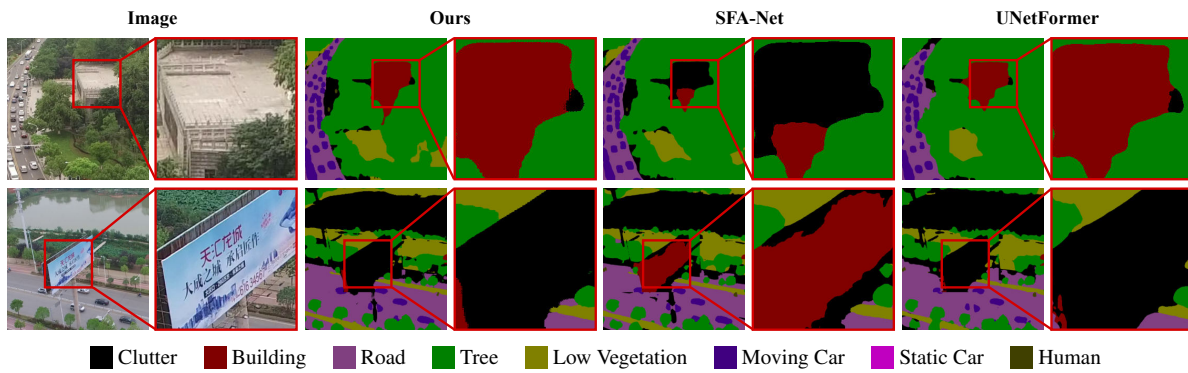


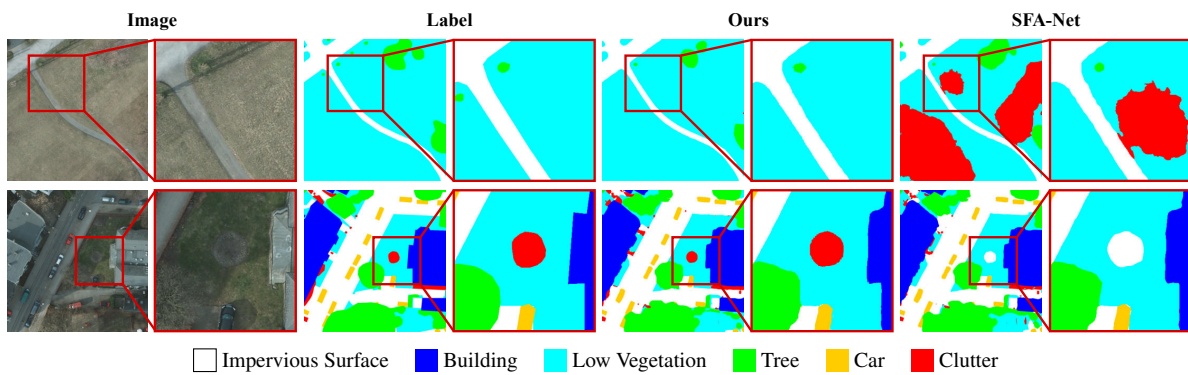
Figure 7. Validation set mIoU trends across all datasets over training epochs.



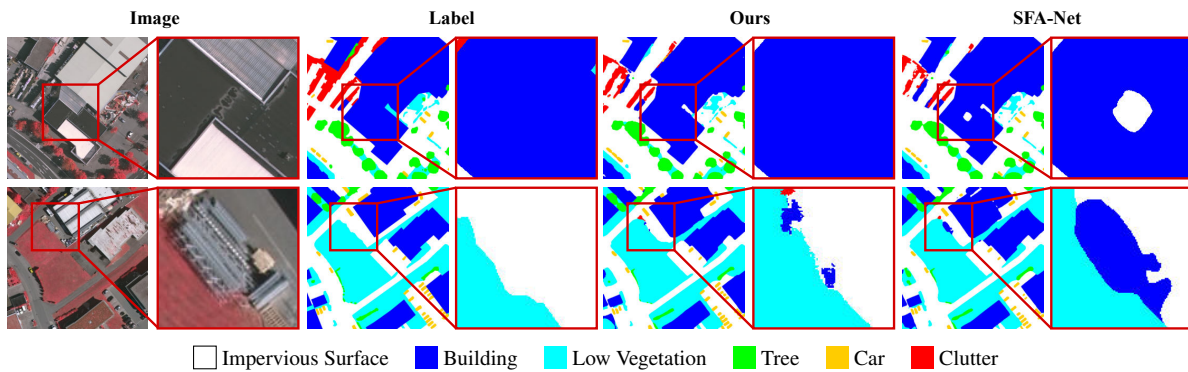
(a) LoveDA



(b) UAVID



(c) Potsdam



(d) Vaihingen

Figure 8. More visualization results of coarse-grained remote sensing images.

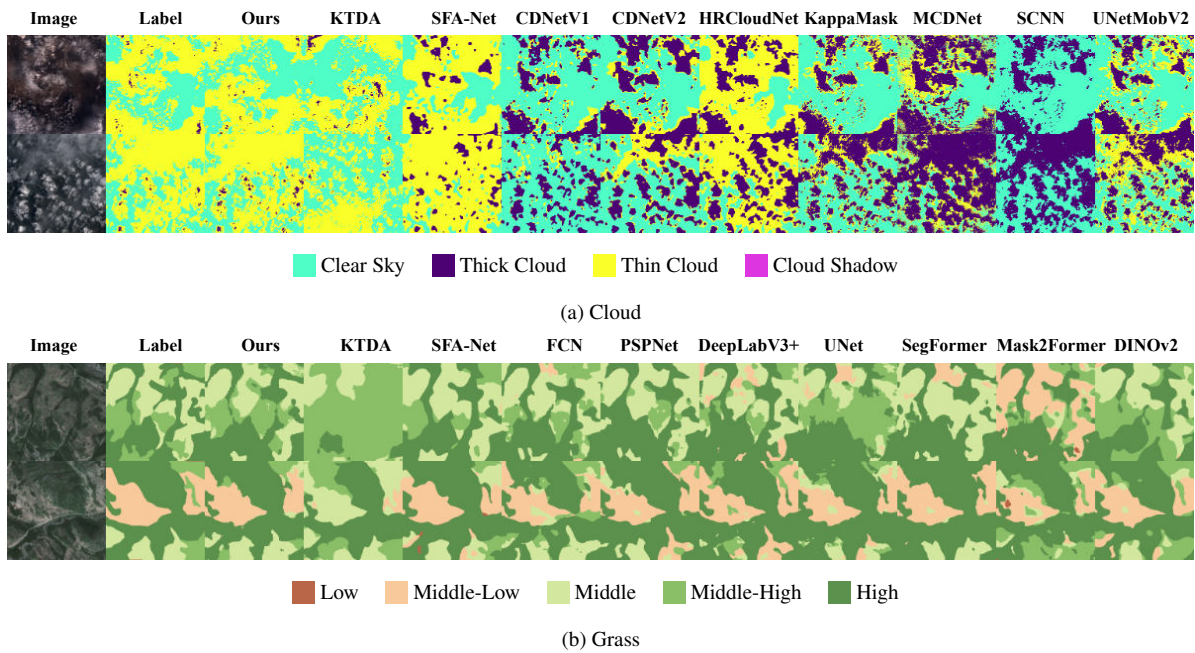


Figure 9. More visualization results of fine-grained remote sensing images.



Figure 10. Visualization examples of bad cases.